Soft Matter

COMMUNICATION

A class of diatomic 2-D soft granular crystals undergoing pattern transformations

Bodhi Rudra,[a] Yunyao Jiang,[b] Yaning Li[b] and Jongmin Shim*[a]

Cite this: *Soft Matter*, 2017, 13, 5824

Received 19th July 2017,
Accepted 17th August 2017

DOI: 10.1039/c7sm01430a

rsc.li/soft-matter-journal

We propose a class of diatomic 2-D soft granular crystals, which features pattern transformation under compression with lateral confinement. The proposed granular crystals are composed of two different types of cylinders: large soft cylinders and small hard cylinders. The pattern-transformable granular crystals are obtained by exploring perturbed packing patterns as potential configurations, and compression with lateral confinement as the driving force of the transition. As a demonstration of the proof-of-concept, we first show the results of desktop-scaled experiments and finite element simulations for a representative case. Then, we present the procedure to obtain these new pattern transformations in soft granular crystals based on the compact packing theory of diatomic circles. The scale-independent compact packing theory serves as an important part of the veiled underlying mechanism of the observed pattern transformations, so the proposed granular crystals can open new avenues in the microstructural design of functional materials towards practical applications.

1 Introduction

Granular crystals (*i.e.*, ordered arrays of particles) are considered as a potential component for energy dissipation[1–4] and a promising configuration for phononic band-gaps.[5–8] In particular, it is reported that the phononic band-structure of a granular crystal can be distinctively altered by its geometry.[7] Thus, the tunability arising from pattern transformations will affect the coverage of the band-gaps, and the versatility of granular crystals can be significantly improved by incorporating pattern transformations. In 2011, Goncu *et al.*[9] reported a deformation-induced pattern transformation of square lattices under compression with lateral confinement (*i.e.*, a kind of biaxial loading condition). They demonstrated a pattern transformation in square arrays of cylindrical particles, and investigated the effect of radius ratio on the pattern transformation and its reversibility. However, since their work, the mechanism of pattern-transformable granular crystals has not been revealed and no other pattern transformation of granular crystals has been suggested or investigated.

Here, we propose four new pattern transformations in soft granular crystals obtained by considering the compact packing of diatomic circles.[10–14] The proposed granular crystals are composed of two different types of cylinders: large soft cylinders and small hard cylinders. The pattern-transformable granular crystals are obtained by exploring perturbed packing patterns as potential configurations, and compression with lateral confinement as the driving force of the transition. As a demonstration of the proof-of-concept, we first show the results of desktop-scaled experiments and finite element (FE) simulations for a representative case. Then, we disclose the procedure to obtain these new pattern transformations in soft granular crystals based on the compact packing theory of diatomic circles. The procedure is composed of two steps. The first step is to identify four potential transformation pairs, which are obtained by considering the packing density evolution under compression with lateral confinement. In the second step, the rigid-body re-arrangement assumption provides the principal compressive loading direction for each transformation potential transformation pair.

2 Experimental results

The cylindrical particles are printed using a 3-D printer, Objet Connex 260, whose printing resolutions is 16 μm. All the printed cylindrical particles have a nominal thickness of T_0 = 6.5 mm. White-colored VeroWhite (Young's modulus E_0^{VW} = 2.00 GPa) is employed to print the hard particles having a nominal radius, r = 2.4 mm. Soft particles are printed with transparent DM60 (*i.e.*, digital material obtained by mixing VeroWhite and TangoPlus, and E_0^{DM60} = 2.49 MPa), and their radius is R = 6.0 mm. Thus, the radius ratio of the particles is $\chi = r/R = 0.40$. The initial

[a] Department of Civil, Structural and Environmental Engineering, University at Buffalo, 240 Ketter Hall, Buffalo, NY 14260, USA. E-mail: jshim@buffalo.edu; Tel: +1-716-645-4372

[b] Department of Mechanical Engineering, University of New Hampshire, 33 College Road, Kingsbury Hall, Durham, NH 03824, USA

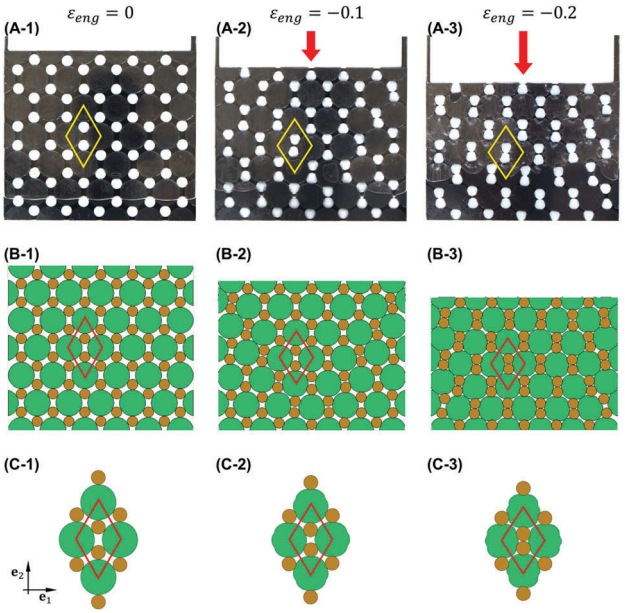

Fig. 1 Pattern transformation of a 2-D soft granular crystal. (A) Experimental results. (B) Finite element (FE) simulation with a full-size model. (C) FE simulation with a unit-cell model with periodic boundary conditions.

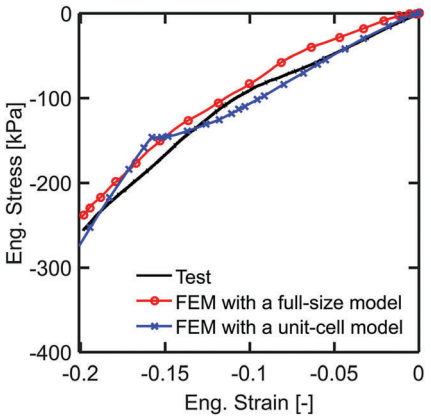

Fig. 2 Stress–strain relation of the 2-D soft granular crystal with the radius ratio of $\chi = r/R = 0.4$.

configuration consists of hard and soft particles placed on rhombic lattices (see Fig. 1A-1), and it can be represented by a rhombic unit-cell, whose major diagonal is straight-up. For the considered granular crystal, we print 66 full hard particles, 27 full soft particles, 12 half-circular soft particles, and 6 soft particles in the shape of a circular segment having a height of 4.73 mm. The non-full soft particles are designed to reduce the contact area between the particles and a surrounding acrylic fixture while maintaining the periodicity of the pattern. Before the assembly of the crystal, all the particles are coated with mineral oil, and Teflon tape is used in the inside of the fixture to further reduce friction between the particles. Using these particles, a granular crystal (width (W_0) × height (H_0) = 84.7 mm × 75.6 mm) is assembled in the acrylic fixture. In this initial configuration, adjacent particles touch each other, but all the particles are uncompressed.

The experiments are performed under compression with lateral confinement, which can be viewed as biaxial loading conditions (see Fig. 1A). With the displacement-controlled setting, the top layer of the granular crystal is compressed at a constant speed of 0.02 mm s^{-1} up to the engineering strain of $\varepsilon_{eng} = -0.20$, where ε_{eng} is the ratio between the applied axial displacement and the initial height of the granular crystal (*i.e.*, H_0). As shown in Fig. 1A-1, all the hard particles are isolated in the initial configuration. Under compression with lateral confinement, however, the granular crystal undergoes particle rearrangement, which leads to a new periodic pattern showing the coalescence of two hard particles (see Fig. 1A-2 and A-3). As the applied load increases, two vertically separated hard particles get closer and they eventually become surrounded by four adjacent soft particles. Fig. 1A-3 shows the deformed shapes of the proposed granular crystal at an engineering strain of $\varepsilon_{eng} = -0.20$, revealing that the unit-cell of the granular crystal remains rhombic under compression with lateral confinement. The observed transition is gradual in time, and slight inhomogeneity over the crystal domain is observed due to the boundary layer. The gradual transition of the pattern is due to the lateral confinement and friction, and it is qualitatively different from the typical bucking behavior showing an abrupt transition. The gradual behavior in pattern transformations can also be seen from the smooth evolution in the stress–stain curve (see Fig. 2).

In addition to the experimental images of the deformed patterns shown in Fig. 1A, we monitor the displacement data and the corresponding load data recorded from the cross-head extension and the load-cell attached to the top layer of the granular crystal, respectively. The engineering stress of σ_{eng} is calculated from the measured force divided by the loading surface area of $W_0 \times T_0$. The stress–strain curve obtained from the experiments is presented with a black solid line in Fig. 2, and we find that stress is monotonically increasing with strain increase. It is worth noticing that, as the compressive strain increases, the overall crystal stiffness (*i.e.*, the slope of the stress–strain curve) of the granular crystal tends to increase due to compaction.

The experimental setting shown in this study contains various types of moderate imperfections, which include particle mis-alignment, non-uniform distribution of lubricants between particles, eccentricity of the vertical loading and boundary effect. Despite these moderate imperfections, we observed repeatable pattern transformation in the experiments, and this experimental finding affirms the robustness of the phenomena under investigation. Furthermore, we focus on the loading transition only in this article, leaving the pattern transformation reversibility upon unloading as the topic of a further investigation. The reversibility of the proposed granular crystals upon unloading is found to be highly affected by the radius ratio as well as the stiffness ratio, and a similar phenomenon was also observed in the square pattern reported by Goncu *et al.*[9]

3 Finite element analysis

Numerical simulations are completed to explore the pattern transformation of the proposed granular crystal. Since soft particles are considered, we perform FE analysis using commercial ABAQUS/Standard software to capture qualitative information of the transition.

The material properties of both soft and hard particles are measured through uniaxial compression testing. A linear elastic model with E_0^{VW} = 2.00 GPa and ν_0^{VW} = 0.4 is employed to represent the material behavior of VeroWhite. On the other hand, the constitutive behavior of DM60 is accurately captured using the Mooney–Rivlin model[15,16] whose strain energy density is $U = C_{10}(\bar{I}_1 - 3) + C_{01}(\bar{I}_2 - 3) + (J-1)^2/D_1$, where C_{10} = 0.174 MPa, C_{01} = 0.243 MPa, and D_1 = 0.0482 MPa^{-1}. Here, $\bar{I}_1 = \mathrm{tr}(J^{-2/3}\mathbf{F}^T\mathbf{F})$, $\bar{I}_2 = \frac{1}{2}\left[\bar{I}_1^2 - \mathrm{tr}\left(J^{-4/3}\left(\mathbf{F}^T\mathbf{F}\right)^2\right)\right]$, $J = \det\mathbf{F}$, and $\mathbf{F}$ is the deformation gradient. The model parameters of Mooney–Rivlin are related to the conventional shear modulus (G_0^{DM60}) and bulk modulus (K_0^{DM60}) at zero strain: $G_0^{DM60} = 2(C_{10} + C_{01})$ and $K_0^{DM60} = 2/D_1$. There are two different sources of friction in experiments: inter-particle friction and friction between particles and the fixture (*i.e.*, side and front walls). In order to consider friction, FE simulations adopt the Coulomb friction model with a friction coefficient of μ = 0.1. In all the FE analyses, 2-D models are constructed using 4-node bilinear plane stress elements with reduced integration (CPS4R elements in ABAQUS/Standard). A series of mesh refinement studies is preformed to assure the independency of numerically obtained load–displacement relations on mesh sizes, and the sweeping mesh size of 0.3 mm is determined to ensure the convergence of the FE simulations.

With these material models and the simulation setting, we execute FE simulations with two different types of models: (i) a full-size model representing the actual experimental setting illustrated in Section 2 and (ii) a unit-cell model with periodic boundary conditions representing an infinitely periodic structure. Fig. 1B shows the pattern transformation of the granular crystal obtained from the FE simulations with the full-size model, and the FE results are in excellent qualitative agreement with the corresponding experiments. Fig. 1B-3 shows the image of the granular crystal at the engineering strain of $\varepsilon_{eng} = -0.2$, where the new patterns are nearly completed showing the coalescence of two hard particles. Moreover, the stress–strain relationship from the FE simulation with the full-size model is presented by the red line with circular marks in Fig. 2, and we observe good quantitative agreement between the experimental and the simulation results. Note that the stress level in the FE simulations is slightly affected by the friction coefficient although the formation of pattern transition is not critically affected by its magnitude.

In addition to the FE simulation with the full-size model, we run computationally inexpensive FE simulations with a unit-cell model with periodic boundary conditions assuming an infinitely periodic structure. Periodic boundary conditions subject to deformation are imposed on the unit-cell by prescribing displacement $\mathbf{u}$ such that $\mathbf{u}_\beta = \mathbf{u}_\alpha + (\bar{\mathbf{F}}^{app} - 1)(\mathbf{X}_\beta - \mathbf{X}_\alpha)$, with the subscripts α and β indicating two nodal points periodically located on unit-cell boundaries, 1 denoting the second order identity tensor, and $\bar{\mathbf{F}}^{app}$ representing the macroscopic deformation gradient imposed on two positions $\mathbf{X}_\alpha$ and $\mathbf{X}_\beta$. Virtual nodes are introduced to prescribe the macroscopic deformation gradient $\bar{\mathbf{F}}^{app}$ at their degrees of freedom. Considering the principle of virtual work, the corresponding macroscopic first Piola–Kirchhoff stress $\bar{\mathbf{P}}^{app}$ can be obtained from the forces at the degree of freedom of the virtual nodes.[17] Specifically, the unit-cell model shown in Fig. 1C-1 is subjected to the macroscopic deformation gradient $\bar{\mathbf{F}}^{app} = \mathbf{e}_1 \otimes \mathbf{e}_1 + (\varepsilon_{eng} + 1)\mathbf{e}_2 \otimes \mathbf{e}_2$. The corresponding nominal stress σ_{eng} is obtained from the corresponding macroscopic first Piola–Kirchhoff stress component $\sigma_{eng} = \bar{\mathbf{P}}_{22}^{app}$. Its detailed implementation for continuum structure modeling can be found in ref. 17–19, and the only change in granular crystal modeling is to include additional boundary layers of particles to impose periodic conditions. In this study, three additional unit-cells are included to model boundary layers, and eventually four primitive unit-cells are employed to model the behavior of one primitive unit-cell subjected to periodic boundary conditions (see Fig. 1C-1). The deformed shapes of the unit-cell model under compression with lateral confinement are presented in Fig. 1C, which depicts its transition to the configuration where two hard particles merge. In addition, Fig. 2 shows that the stress–strain relation from the unit-cell model simulation is well compared with the experimental results and the FE predictions with the full-size model. Note that the evolution of its overall stiffness is not as monotonic as the one from the full-size model. In the unit-cell model simulation, a rather abrupt stiffness change occurs around $\varepsilon_{eng} \sim -0.15$ when the two hard particles touch each other. On the other hand, the full-size model includes approximately 30 primitive unit-cells (see Fig. 1B) and its nonlinear behavior is nonhomogeneous, so the onset of two-hard-particle contacts spreads over a range of applied strains, resulting in a smooth monotonic evolution of the overall crystal stiffness. In general, we find that the deformed shapes and the corresponding stress–strain relation of the unit-cell model show good agreement with the experimental results and the full-size model FE predictions, as shown in Fig. 1C and 2, respectively.

Given the good qualitative and quantitative agreement found among the full-size model, the unit-cell model, and the experimental results, we proceed by focusing on FE analysis with the unit-cell models to further discuss how to obtain a class of new pattern-transformable granular crystals.

4 Pattern-transformable granular crystals from diatomic circular packing

Through a combination of experiments and FE simulations, we have demonstrated the proof-of-concept of the new pattern-transformable granular crystal under compression with lateral confinement. We now present the procedure to obtain a class of new pattern-transformable granular crystals. In the granular crystal reported by Goncu *et al.*,[9] hard and soft particles are initially placed on two embedded square lattices, and the pattern transformation is observed upon compression with lateral confinement.

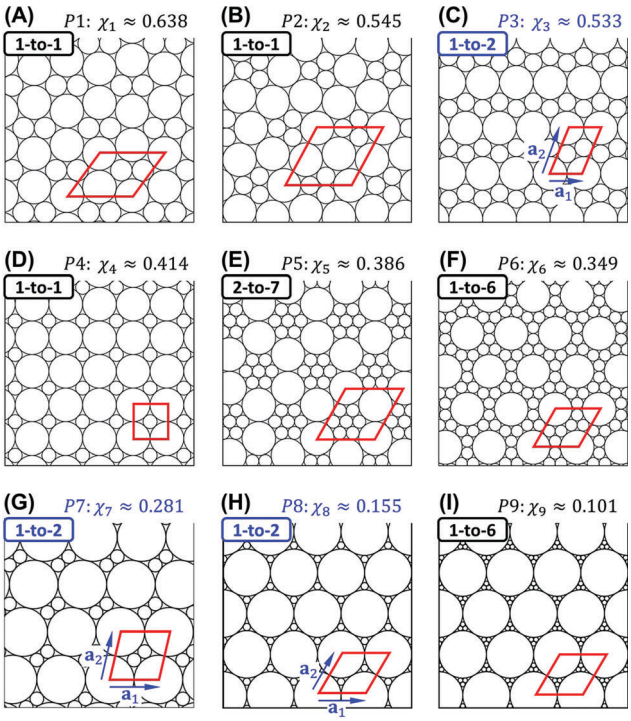

Fig. 3 The complete list of 9 compact diatomic circles, denoted by $P1,\ldots,P9$. Each pattern shows the radius ratio (*i.e.*, $\chi = r/R$) and the particle ratio (*i.e.*, the ratio between the number of large circles and the number of small circles in a primitive unit-cell delineated by a red-colored rhombus). For the configurations having a 1-to-2 particle ratio, primitive lattice vectors $\mathbf{a}_1$ and $\mathbf{a}_2$ are also denoted.

During the transition of the granular crystal, we observe an increase in packing density, which is defined as the ratio of particle area within a unit-cell to the unit-cell area and is denoted by ψ in this study. Motivated by this observation, we examine the compact packing density theory of diatomic circles[10–14] in order to search for other pattern-transformable granular crystals. The compact packing of circles is defined as a condition where every pair of circles in contact is in mutual contact with two other circles.[10,13] For diatomic circles, Kennedy[13] identified the complete list of 9 compact radius ratios (denoted by $\chi_1,\ldots,\chi_9$) and the corresponding compact packing (denoted by $P1,\ldots,P9$), as presented in Fig. 3. In addition, by slightly changing the radius ratio (*i.e.*, $\chi = r/R$) near each compact packing, he also introduced the corresponding perturbed packing configuration (denoted by $P1',\ldots,P9'$). Fig. 4 illustrates a few of the perturbed patterns $P3'$, $P7'$, and $P8'$ obtained from the compact packing configurations. Note that most compact packing configurations (*e.g.*, $P3$, $P7$) have two different contact conditions for their perturbed packing configuration: one below and the other above the compact radius ratio. However, some compact packing configurations (*e.g.*, $P8$) have only one type of perturbed packing above its compact radius ratio because small particles lose contact with the surrounding large particles in a configuration having the radius ratio smaller than the compact radius ratio (*e.g.*, see Fig. 4C for $P8'$).

Based on the list of the diatomic compact packing, the pattern-transformable granular crystal reported by Goncu *et al.*[9] can be viewed as a transition between two perturbed packing configurations. In other words, the initial square pattern is a perturbed packing $P4'$, and the re-arranged (*i.e.*, final) configuration under compression with lateral confinement is a perturbed packing $P1'$ (see Fig. 3). Inspired by this finding, we seek new pattern transformations by exploring the perturbed packing as potential pattern-transformable configurations, and compression with lateral confinement as the driving force of the transition. The exploration now requires us to resolve two principle questions: how to identify a proper transformation pair of configurations and how to find a proper set of loading directions and radius ratios.

4.1 Transformation pairs

To identify a potential transformation pair of configurations, we consider the ratio between the number of large circles and the number of small circles in a primitive unit-cell, *i.e.*, $N_{\text{large circles}} : N_{\text{small circles}}$, which is referred to as the particle ratio in this study. During the transition under compression with lateral confinement, the particle ratio of a considered granular crystal should not be changed. Thus, we re-visit the complete list of the diatomic compact packing configurations (see Fig. 3), and then arrange them in groups using the particle ratio within a primitive unit-cell. There exist four groups of packing configurations: (1) 1-to-1: $P1$, $P2$, $P4$; (2) 1-to-2: $P3$, $P7$, $P8$; (3) 1-to-6: $P6$, $P9$; and (4) 2-to-7: $P5$. The particle ratio for each pattern is also denoted in Fig. 3. Multiple transformation pairs may exist within these groups, but we focus on the particle ratio of 1-to-2 in this study.

For a given packing arrangement with soft granular particles, the packing density should increase upon compression with lateral confinement. In other words, for a given radius ratio χ, the packing density of the initial configuration should be lower than that of the re-arranged configuration under compression with lateral confinement. Thus, for each compact packing in the group of the 1-to-2 particle ratio, we obtain the analytical expressions of the packing density of the corresponding perturbed packing as follows:

$$\psi^{P3'}(\chi) = \begin{cases} \dfrac{\pi}{2}\,\dfrac{1+2\chi^2}{1+\chi+\sqrt{\chi(\chi+2)}} & \chi \in [0.155,\ 0.533] \\ \dfrac{\pi}{8}\,\dfrac{(1+2\chi^2)(1+\chi)^2}{\chi(1+2\chi)\sqrt{1+2\chi}} & \chi \in [0.533,\ 1] \end{cases}, \quad (1)$$

$$\psi^{P7'}(\chi) = \begin{cases} \dfrac{\pi}{8}\,\dfrac{(1+2\chi^2)(1+\chi)^2}{\sqrt{\chi(\chi+2)}} & \chi \in [0.155,\ 0.281] \\ \dfrac{\pi}{2}\,\dfrac{1+2\chi^2}{(1+2\chi)\sqrt{1+2\chi}} & \chi \in [0.281,\ 1] \end{cases}, \quad (2)$$

$$\psi^{P8'}(\chi) = \frac{2\pi}{3\sqrt{3}}\frac{1+2\chi^2}{(1+\chi)^2} \quad \chi \in [0.155,\ 1]. \quad (3)$$

The above analytical expressions are derived by considering two different contact conditions of each perturbed packing, except

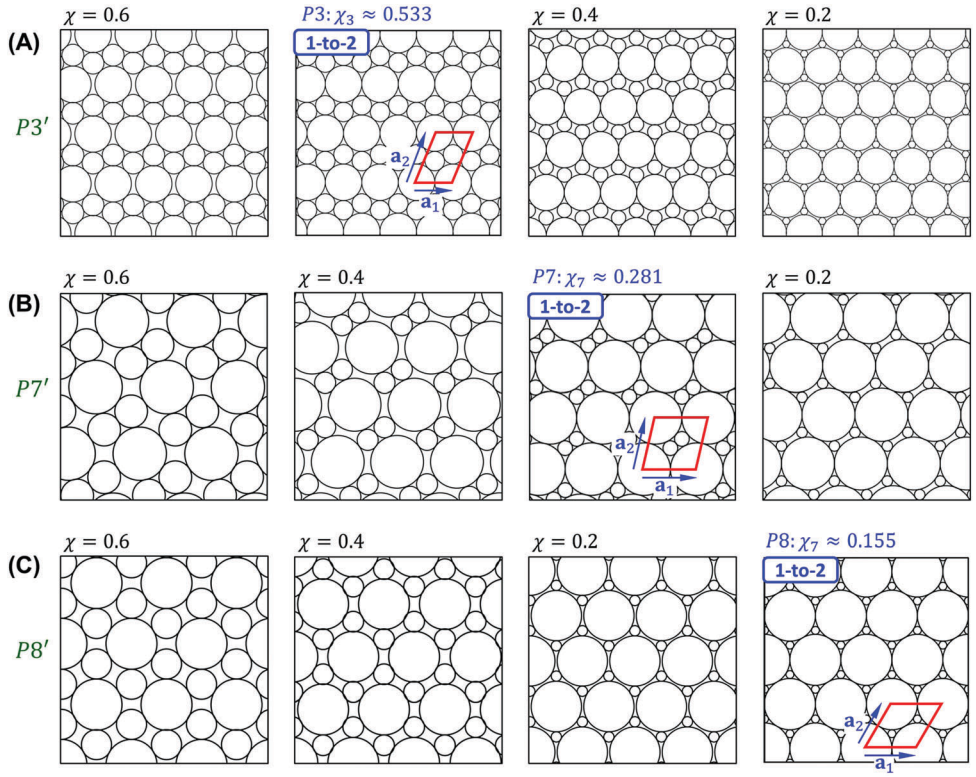

Fig. 4 Examples of perturbed patterns for the packing configurations having the particle ratio of 1-to-2. (A) Perturbed patterns *P*3′. (B) Perturbed patterns *P*7′. (C) Perturbed patterns *P*8′.

for *P*8′ (see Fig. 4). Fig. 5 shows the evolution of packing density in terms of the radius ratio χ. By way of illustration, consider the particle configuration for the compact packing *P*3 having $\chi_3 \approx 0.533$ and $\psi \approx 0.914$ (see Fig. 4A for its pattern). As the radius ratio χ decreases, the configuration deviates from the compact packing *P*3, reducing its packing density to $\psi \approx 0.867$ at $\chi \approx 0.344$. The further decrease to $\chi = \chi_8 \approx 0.155$ eventually results in the compact packing *P*8. Similarly, the increase in the radius ratio χ also provides the evolution of its packing density, and leads to the monatomic hexagonal packing at $\chi = 1$.

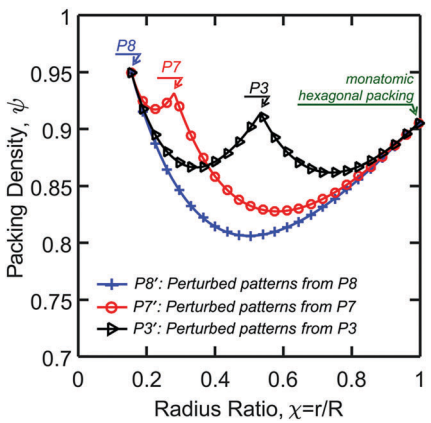

Fig. 5 The evolution of packing density of diatomic perturbed patterns in terms of the radius ratio, χ.

The other two types of perturbed patterns also show similar evolutions. Fig. 5 shows that the family of perturbed packing configurations *P*8′ possesses the least packing density for any given radius ratio. Thus, under compression with lateral confinement, the perturbed packing configurations *P*8′ are inadequate for the re-arranged (*i.e.*, final) configuration since the packing density of the initial configuration should be lower than that of the re-arranged configuration. There exist six transformation pairs from the permutation of three perturbed packing configurations (*i.e.*, *P*3′, *P*7′, and *P*8′), but we exclude two cases which include *P*8′ as the re-arranged configuration. Consequently, the consideration of packing density evolution under compression with lateral confinement provides four potential transformation pairs: (a) *P*8′ to *P*7′, (b) *P*8′ to *P*3′, (c) *P*7′ to *P*3′, and (d) *P*3′ to *P*7′.

4.2 Loading direction and radius ratio

For the identified potential transformation pairs, a systematic analytical study is performed to find proper radius ratios and the corresponding loading directions. For a given radius ratio χ, there exist three different perturbed configurations, *i.e.*, *P*3′, *P*7′, and *P*8′. A proper loading direction for pattern transformations among those configurations has to be related to the applied macroscopic deformation gradient $\bar{\mathbf{F}}^{\mathrm{app}}$. For a given radius ratio, we estimate a macroscopic deformation gradient by comparing the geometry of the initial and re-arranged primitive unit-cells.[20] Operationally, assuming rigid-body

re-arrangements, we obtain a macroscopic deformation gradient $\bar{\mathbf{F}}$ considering the unit-cells delineated in Fig. 4:

$$\bar{\mathbf{F}}\mathbf{a}_1^i = \mathbf{a}_1^r, \quad \bar{\mathbf{F}}\mathbf{a}_2^i = \mathbf{a}_2^r \Rightarrow \bar{\mathbf{F}} = [\mathbf{a}_1^r\mathbf{a}_2^r][\mathbf{a}_1^i\mathbf{a}_2^i]^{-1}, \tag{4}$$

where $\mathbf{a}_1$ and $\mathbf{a}_2$ indicate the primitive lattice vectors of the considered configurations (see Fig. 4), and the superscripts i and r indicate the initial and the re-arranged configurations, respectively. Subsequently, we perform the polar decomposition of the macroscopic deformation gradient, $\bar{\mathbf{F}} = \bar{\mathbf{R}}\bar{\mathbf{U}}$, where $\bar{\mathbf{R}}$ is the macroscopic rotation tensor and $\bar{\mathbf{U}}$ is the macroscopic right stretch tensor.[21] Then, the principle compressive loading direction (*i.e.*, measured by an angle θ from the horizontal direction in the initial configuration) is obtained by taking the eigen-decomposition of $\bar{\mathbf{U}}$, *i.e.*$\bar{\mathbf{U}} = \bar{\mathbf{Q}}\bar{\mathbf{U}}^{\star}\bar{\mathbf{Q}}^{\mathrm{T}}$, where $\bar{\mathbf{U}}^{\star}$ is the principal macroscopic right stretch tensor and $\bar{\mathbf{Q}}$ is the coordinate transformation matrix represented by $\bar{\mathbf{Q}} = [\cos(-\theta), \sin(-\theta); -\sin(-\theta), \cos(-\theta)]$. Thus, for a given set of radius ratios χ and a transformation pair, the principle compressive loading direction θ can be explicitly obtained. Fig. 6 illustrates the identified loading directions for each potential transformation pair. The compressive loading angle of the transitions $P8' \rightarrow P7'$ and $P8' \rightarrow P3'$ is independent of the radius ratio and is found to be $\theta = 30^\circ$ and 0°, respectively. For the transitions $P7' \rightarrow P3'$ and $P3' \rightarrow P7'$, however, the compressive loading angle depends on the radius ratio.

With the constructed principle loading direction for each transformation pair, we perform a series of parametric FE simulations with a unit-cell model by sweeping the radius ratio, $\chi \in [0.155, 1]$. For a desired principle stretch $\bar{\mathbf{U}}^{\star\mathrm{app}}$ in the principle loading direction, the deformation gradient $\bar{\mathbf{F}}^{\mathrm{app}}$ to be applied in the initial configuration of the considered unit-cell is determined from $\bar{\mathbf{F}}^{\mathrm{app}} = \bar{\mathbf{Q}}\bar{\mathbf{U}}^{\star\mathrm{app}}\bar{\mathbf{Q}}^{\mathrm{T}}$. Furthermore, we extract the corresponding engineering stress from the transformed macroscopic first Piola–Kirchhoff stress, $\bar{\mathbf{P}}^{\star\mathrm{app}} = \bar{\mathbf{Q}}^{\mathrm{T}}\bar{\mathbf{P}}^{\mathrm{app}}\bar{\mathbf{Q}}$. For each transition pair, we find a narrow range of the radius ratio χ resulting in a distinctive pattern transformation: (a) $P8'$ to $P7'$: $\chi \in [0.20, 0.46]$ with $\theta = 30^\circ$, (b) $P8'$ to $P3'$: $\chi \in [0.40, 0.60]$ with $\theta = 0^\circ$, (c) $P7'$ to $P3'$: $\chi \in [0.40, 0.60]$ with $\theta \in [-23^\circ, -8.3^\circ]$, and (d) $P3'$ to $P7'$: $\chi \in [0.20, 0.46]$ with $\theta \in [45.9^\circ, 72.3^\circ]$. In Fig. 6, the radius ratios leading to pattern transformation are denoted by solid lines with markers.

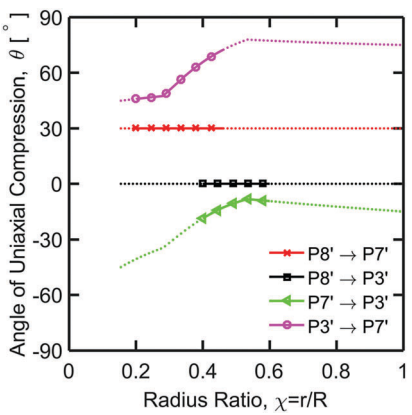

Fig. 6 The principle compressive loading direction for the four transition pairs based on the rigid body re-arrangements. The solid lines with markers denote the loading angles which lead to a distinctive pattern transformation.

In order to provide the representative FE analysis results using unit-cells with periodic boundary conditions, we select the radius ratio of $\chi = 0.4$ in this study. Fig. 7 shows the initial and the deformed shapes of each transition pair under the corresponding loading direction. At the strain level of $\varepsilon_{\mathrm{eng}} = -0.3$, the pattern transformation is nearly completed for each case. The corresponding stress–strain relations is also presented in Fig. 8. Due to compaction, the overall crystal stiffness is increasing as the compressive strain increases. Furthermore, for the identified geometric and loading configurations of pattern transformations, we explore the size-effect of an enlarged unit-cell model, whose area is enclosed by lattice vectors $m_1\mathbf{a}_1$ and $m_2\mathbf{a}_2$. Fig. 9 and 10 show the FE analysis results employing an enlarged unit-cell with $m_1 = m_2 = 5$. We find that the pattern transformation observed in the enlarged unit-cell simulations are also well compared with the results from the primitive unit-cell simulations having $m_1 = m_2 = 1$. Note that the macroscopic deformation gradient $\bar{\mathbf{F}}^{\mathrm{app}}$ is imposed only on unit-cell boundaries, and the motion of the unit-cell inner part is indirectly governed by the constraints on unit-cell boundaries. Thus, by increasing the

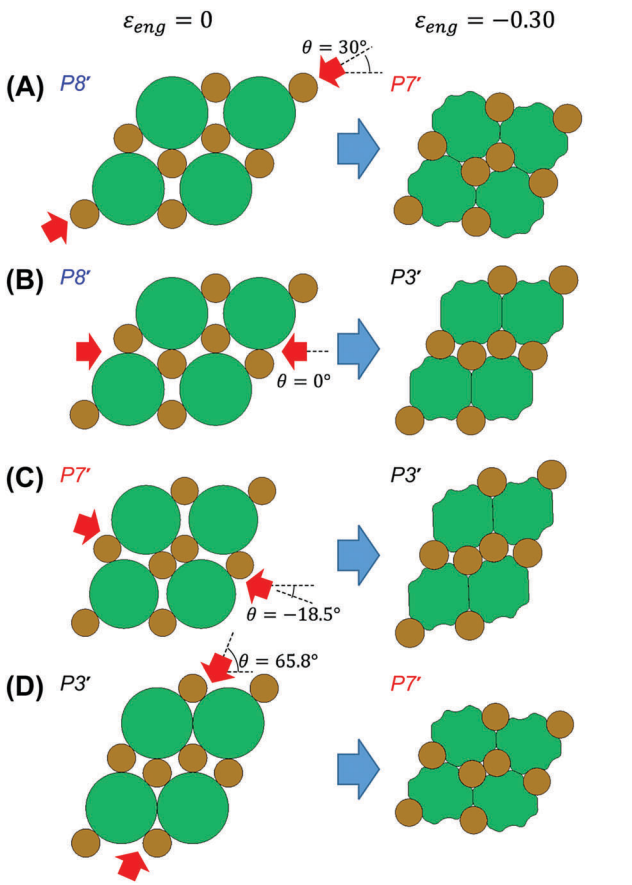

Fig. 7 FE simulation results using unit-cells enclosed by lattice vectors $\mathbf{a}_1$ and $\mathbf{a}_2$. The radius ratio is $\chi = 0.4$. (A) $P8'$ to $P7'$. (B) $P8'$ to $P3'$. (C) $P7'$ to $P3'$. (D) $P3'$ to $P7'$.

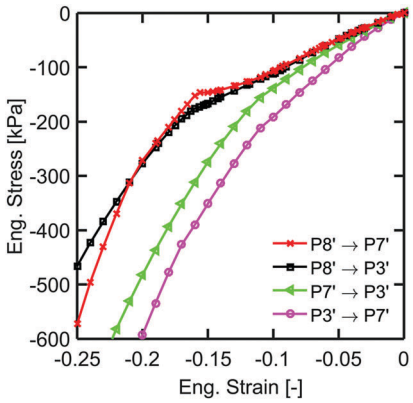

Fig. 8 Stress–strain relation obtained from FE simulation using unit-cells enclosed by lattice vectors $\mathbf{a}_1$ and $\mathbf{a}_2$. The radius ratio is $\chi = 0.4$.

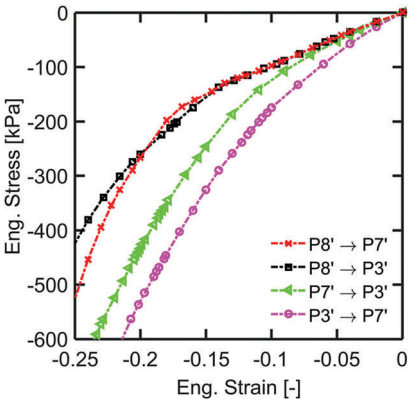

Fig. 10 Stress–strain relation obtained from FE simulation using unit-cells enclosed by lattice vectors $5\mathbf{a}_1$ and $5\mathbf{a}_2$. The radius ratio is $\chi = 0.4$.

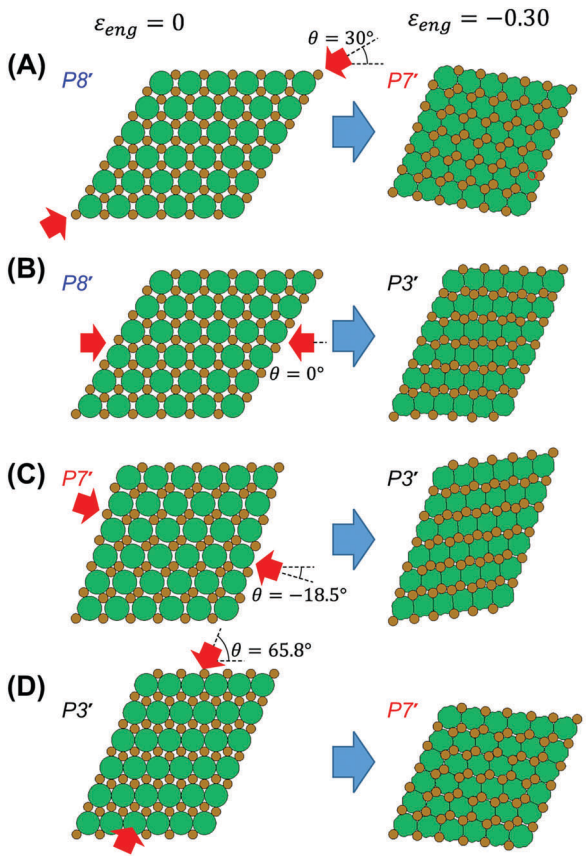

Fig. 9 FE simulation results using unit-cells enclosed by lattice vectors $5\mathbf{a}_1$ and $5\mathbf{a}_2$. The radius ratio is $\chi = 0.4$. (A) $P8'$ to $P7'$. (B) $P8'$ to $P3'$. (C) $P7'$ to $P3'$. (D) $P3'$ to $P7'$.

size of the enlarged unit-cell in FE simulations, the employed numerical formulation introduces more inhomogeneity under loading conditions, which can be viewed as a type of numerical imperfection in loading. Consequently, the pattern transformation observed in the enlarged unit-cell models numerically affirms the robustness of the phenomena under investigation, but only to a modest extent. In Sections 2 and 3, we choose the transition $P8'$ to $P7'$ with $\chi = 0.4$ to demonstrate the proof-of-concept of the proposed pattern-transformable granular crystals. The initial configuration of the considered crystal (*i.e.*, the pattern $P8'$) is designed such that the principle compressive loading direction is aligned with the vertical loading direction of the universal testing machine.

5 Conclusion

In this study, we introduce a class of pattern-transformable diatomic 2-D soft granular crystals, whose transition is induced by compression with lateral confinement. The proof-of-concept of the proposed granular crystals is demonstrated by performing a combination of experiments and numerical simulations with a finite size specimen. Furthermore, based on the compact packing theory of diatomic circles, we present a systematic procedure to obtain these new pattern transformations in soft granular crystals. Pattern transformations in soft granular crystals are due to various factors including material properties, friction coefficients, loading rates, geometry/material imperfections, particle configurations, *etc.* In this study, we demonstrate that the particle configuration (or compact packing) is an important part of the veiled pattern transformation mechanism.

The scale-independent compact packing theory serves as an underlying mechanism of the observed pattern transformations, so the proposed granular crystals can open new avenues in the microstructural design of functional materials towards practical applications. In this study, deformation is used as the driving force of the pattern transformations. However, as seen in research activities in continuum structures,[22–25] the proposed pattern transformations can also be initiated by several other driving forces such as swelling/shrinking actuation under various external stimuli including pH, temperature, and water content. Furthermore, it is well known that the band-structure and wave characteristics of phononic crystals are significantly affected by their geometry and material nonlinearity.[26,27] Thus, the proposed pattern-transformable granular crystals can open the possibility of tunable phononic crystals actuated by various driving forces.

On the other hand, the proposed configurations possess various aspects to be further investigated. This study has not

explored the reversibility upon unloading and the effect of imperfections, and they are the next topics for further investigations. Moreover, in addition to the compact packing of particles, we are currently studying the instability of particle configurations as another key ingredient of the proposed transitions.

Conflicts of interest

All the authors declare that there is no conflict of interest with any financial organization regarding the material discussed in the manuscript.

Acknowledgements

This work has been partially supported by the National Science Foundation through Grant CMMI-1649111. Shim acknowledges start-up funds from the University at Buffalo (UB), and he is grateful to the support of UB Center for Computational Research. Li acknowledges NSF through grants CMMI-1554468 (CAREER), and start-up funds from the University of New Hampshire (UNH). Jiang acknowledges the CEPS fellowship at UNH. We also acknowledge Joe Beckwith at UNH for the help on experiments.

References

1 Y. Nahmad-Molinari and J. Ruiz-Suarez, Epitaxial growth of granular single crystals, *Phys. Rev. Lett.*, 2002, **89**, 264302.
2 Y. Starosvetsky, Evolution of the primary pulse in one-dimensional granular crystals subject to on-site perturbations: Analytical study, *Phys. Rev. E: Stat., Nonlinear, Soft Matter Phys.*, 2012, **85**, 051306.
3 M. Gonzalez, J. Yang, C. Daraio and M. Ortiz, Mesoscopic approach to granular crystal dynamics, *Phys. Rev. E: Stat., Nonlinear, Soft Matter Phys.*, 2012, **85**, 016604.
4 A. Leonard, F. Fraternali and C. Daraio, Directional Wave Propagation in a Highly Nonlinear Square Packing of Spheres, *Exp. Mech.*, 2013, **53**(3), 327–337.
5 E. B. Herbold, J. Kim, V. F. Nesterenko, S. Y. Wang and C. Daraio, Pulse propagation in a linear and nonlinear diatomic periodic chain: effects of acoustic frequency band-gap, *Acta Mech.*, 2009, **205**(1–4), 85–103.
6 H. Pichard, A. Duclos, J. P. Groby, V. Tournat and V. E. Gusev, Two-dimensional discrete granular phononic crystal for shear wave control, *Phys. Rev. B: Condens. Matter Mater. Phys.*, 2012, **86**(13), 134307.
7 F. Goncu, S. Luding and K. Bertoldi, Exploiting pattern transformation to tune phononic band gaps in a two-dimensional granular crystal, *J. Acoust. Soc. Am.*, 2012, **131**(6), EL475–EL480.
8 F. Allein, V. Tournat, V. E. Gusev and G. Theocharis, Tunable magneto-granular phononic crystals, *Appl. Phys. Lett.*, 2016, **108**(16), 161903.
9 F. Goncu, S. Willshaw, J. Shim, J. Cusack, S. Luding, T. Mullin and K. Bertoldi, Deformation induced pattern transformation in a soft granular crystal, *Soft Matter*, 2011, **7**(6), 2321–2324.
10 L. F. Toth, *Regular Figures*, Macmillan, 1964.
11 C. Likos and C. Henley, Complex alloy phases for binary hard-disc mixtures, *Philos. Mag. B*, 1993, **68**(1), 85–113.
12 P. Leung, C. Henley and G. Chester, Dodecagonal order in a two-dimensional lennard-jones system, *Phys. Rev. B: Condens. Matter Mater. Phys.*, 1989, **39**(1), 446–458.
13 T. Kennedy, Compact packings of the plane with two sizes of discs, *Discrete & Computational Geometry*, 2006, vol. 35(2), pp. 255–267.
14 T. Kennedy, Diatomic Circle Packings. http://math.arizona.edu/tgk/pack_two_discs/.
15 M. Mooney, A theory of large elastic deformation, *J. Appl. Phys.*, 1940, **11**, 582–592.
16 R. S. Rivlin, Large elastic deformations of isotropic materials. iv. further developments of the general theory, *Philos. Trans. R. Soc., A*, 1948, **241**, 379.
17 M. Danielsson, D. M. Parks and M. C. Boyce, Three-dimensional micromechanical modeling of voided polymeric materials, *J. Mech. Phys. Solids*, 2002, **50**, 351–379.
18 K. Bertoldi, M. Boyce, S. Deschanel, S. Prange and T. Mullin, Mechanics of deformation-triggered pattern transformations and superelastic behavior in periodic elastomeric structures, *J. Mech. Phys. Solids*, 2008, **56**, 2642–2668.
19 J. Shim, P. Wang and K. Bertoldi, Harnessing instability-induced pattern transformation to design tunable phononic crystals, *Int. J. Solids Struct.*, 2015, **58**(1), 52–61.
20 D. Mohr and M. Oswald, A new experimental technique for the multi-axial testing of advanced high strength steel sheets, *Exp. Mech.*, 2008, **48**(1), 65–77.
21 G. A. Holzapfel, *Nonlinear Solid Mechanics: A Continuum Approach for Engineering*, John Wiley & Sons, LTD, 2000.
22 G. Stoychev, S. Zakharchenko, S. Turcaud, J. W. C. Dunlop and L. Ionov, Shape-Programmed Folding of Stimuli-Responsive Polymer Bilayers, *ACS Nano*, 2012, **6**(5), 3925–3934.
23 S. H. Kang, S. Shan, A. Kosmrlj, W. L. Noorduin, S. Shian, J. C. Weaver, D. R. Clarke and K. Bertoldi, Complex Ordered Patterns in Mechanical Instability Induced Geometrically Frustrated Triangular Cellular Structures, *Phys. Rev. Lett.*, 2014, **112**(9), 098701.
24 J. M. Boothby and T. H. Ware, Dual-responsive, shape-switching bilayers enabled by liquid crystal elastomers, *Soft Matter*, 2017, **13**(24), 4349–4356.
25 S. Xiao, Y. Yang, M. Zhong, H. Chen, Y. Zhang, J. Yang and J. Zheneg, Salt-Responsive Bilayer Hydrogels with Pseudo-Double-Network Structure Actuated by Polyelectrolyte and Antipolyelectrolyte Effects, *ACS Appl. Mater. Interfaces*, 2017, **9**(24), 20843–20851.
26 P. Wang, J. Shim and K. Bertoldi, Effects of geometric and material nonlinearities on tunable band gaps and low-frequency directionality of phononic crystals, *Phys. Rev. B: Condens. Matter Mater. Phys.*, 2013, **88**(1), 014304.
27 A. Leonard and C. Daraio, Stress Wave Anisotropy in Centered Square Highly Nonlinear Granular Systems, *Phys. Rev. Lett.*, 2012, **108**(21), 214301.